LETTER

Single–layer MoS$_2$ nanopores as nanopower generators

Jiandong Feng[1], Michael Graf[1], Ke Liu[1], Dmitry Ovchinnikov[2], Dumitru Dumcenco[2], Mohammad Heiranian[3], Vishal Nandigana[3], Narayana R. Aluru[3], Andras Kis[2] & Aleksandra Radenovic[1]

Making use of the osmotic pressure difference between fresh water and seawater is an attractive, renewable and clean way to generate power and is known as 'blue energy'[1–3]. Another electrokinetic phenomenon, called the streaming potential, occurs when an electrolyte is driven through narrow pores either by a pressure gradient[4] or by an osmotic potential resulting from a salt concentration gradient[5]. For this task, membranes made of two-dimensional materials are expected to be the most efficient, because water transport through a membrane scales inversely with membrane thickness[5–7]. Here we demonstrate the use of single-layer molybdenum disulfide (MoS$_2$) nanopores as osmotic nanopower generators. We observe a large, osmotically induced current produced from a salt gradient with an estimated power density of up to 10^6 watts per square metre—a current that can be attributed mainly to the atomically thin membrane of MoS$_2$. Low power requirements for nanoelectronic and optoelectric devices can be provided by a neighbouring nanogenerator that harvests energy from the local environment[8–11]—for example, a piezoelectric zinc oxide nanowire array[8] or single-layer MoS$_2$ (ref. 12). We use our MoS$_2$ nanopore generator to power a MoS$_2$ transistor, thus demonstrating a self-powered nanosystem.

MoS$_2$ nanopores have already demonstrated better water-transport behaviour than graphene[13,14] owing to the enriched hydrophilic surface sites (provided by the molybdenum) that are produced following either irradiation with transmission electron microscopy (TEM)[15] or electrochemical oxidation[16]. The osmotic power is generated by separating two reservoirs containing potassium chloride (KCl) solutions of different concentrations with a freestanding MoS$_2$ membrane, into which a single nanopore has been introduced[13]. A chemical potential gradient arises at the interface of these two liquids at a nanopore in a 0.65-nm-thick, single-layer MoS$_2$ membrane, and drives ions spontaneously across the nanopore, forming an osmotic ion flux towards the equilibrium state (Fig. 1a). The presence of surface charges on the pore screens the passing ions according to their charge polarity, and thus results in a net measurable osmotic current, known as reverse electrodialysis[1]. This cation selectivity can be better understood by analysing the concentration of each ion type (potassium and chloride) as a function of the radial distance from the centre of the pore, as we show here through molecular-dynamics simulations (Fig. 1b).

We fabricated MoS$_2$ nanopores either by TEM[13] (Fig. 1c) or by the recently demonstrated electrochemical reaction (ECR) technique[16]. With a typical nanopore diameter in the range 2–25 nm, a stable
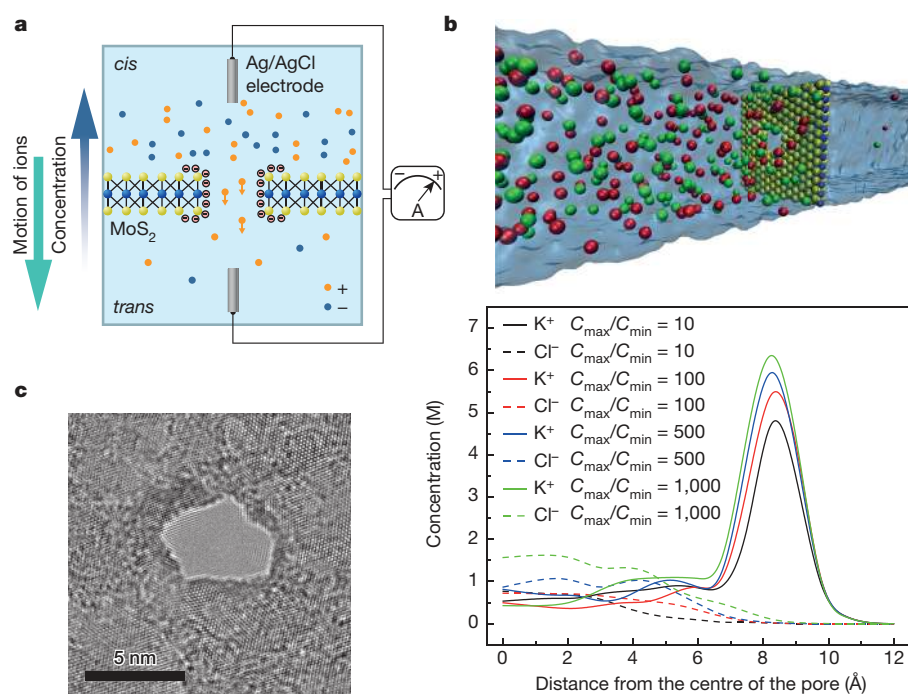

Figure 1 | Harvesting osmotic energy with MoS$_2$ nanopores. a, The experimental set-up. Salt solutions with different concentrations are separated by a 0.65-nm-thick MoS$_2$ nanopore membrane. An ion flux driven by chemical potential through the pore is screened by the negatively charged pore, forming a diffusion current composed of mostly positively charged ions. **b**, Top panel, a typical simulation box used in molecular-dynamics simulations, showing the nanopore membrane (in blue and yellow) and the salt (green and red) in solution. Bottom panel, molecular-dynamics-simulated potassium-ion and chloride-ion concentrations as a function of the radial distance from the centre of the pore. The region near the charged wall of the pore is representative of the electrical double layer. C_{max}, maximum concentration; C_{min}, minimum concentration. **c**, Example of a TEM-drilled MoS$_2$ nanopore of diameter 5 nm.

[1]Laboratory of Nanoscale Biology, Institute of Bioengineering, School of Engineering, EPFL, 1015 Lausanne, Switzerland. [2]Laboratory of Nanoscale Electronics and Structures, Institute of Electrical Engineering and Institute of Materials Science and Engineering, School of Engineering, EPFL, 1015 Lausanne, Switzerland. [3]Department of Mechanical Science and Engineering, Beckman Institute for Advanced Science and Technology, University of Illinois at Urbana-Champaign, Urbana, Illinois 61801, USA.
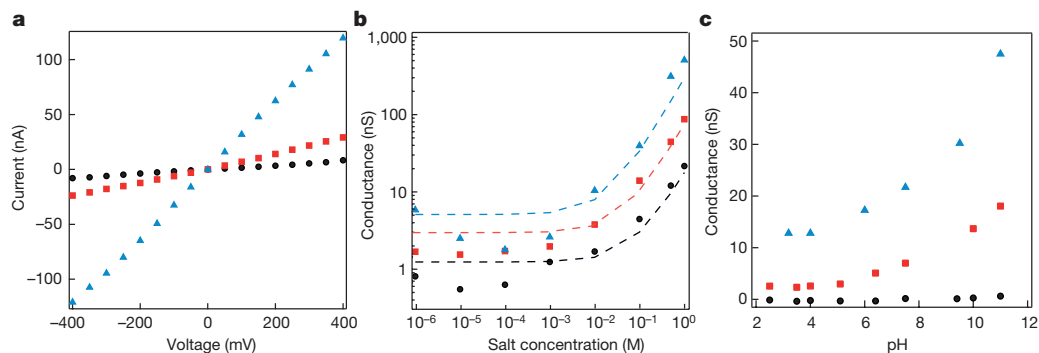
Figure 2 | Electrical conductance and chemical reactivity of the MoS₂ nanopore. a, Current–voltage response of MoS₂ nanopores with different pore sizes (black, 2 nm; red, 6 nm; blue, 25 nm) in 1 M KCl at pH 5. **b**, Conductance as a function of salt concentration at pH 5. By fitting the results to equation (1), we find the extracted surface charge values to be $-0.024\ \mathrm{C\,m^{-2}}$, $-0.053\ \mathrm{C\,m^{-2}}$ and $-0.088\ \mathrm{C\,m^{-2}}$ for a 2-nm, 6-nm and 25-nm pore, respectively. **c**, Conductance as a function of pH for a KCl concentration of 10 mM, for a 2-nm, 6-nm and 25-nm pore.

osmotic current can be expected, owing to the long time required for the system to reach equilibrium. We measured the osmotic current and voltage across the pore by using a pair of Ag/AgCl electrodes to characterize the current–voltage (I–V) response of the nanopore.

To gain a better insight into the performance of the MoS₂ nanopore power generator, we first characterized the ionic transport properties of MoS₂ nanopores under various ionic concentrations and pH conditions, which can provide information on the surface charge of the MoS₂ nanopore. Figure 2a shows the I–V characteristics of MoS₂ nanopores of various diameters. A large pore conductance originates from the ultrathin nature of the membrane. The conductance also depends on the salt concentration (Fig. 2b) and shows saturation at low salt concentrations—a signature of the presence of surface charge on the nanopore[17,18]. The predicted pore conductance (G), taking into account the contribution of the surface charge (Σ), is given by[19]:

$$G = \kappa_b \left[\frac{4L}{\pi d^2} \times \frac{1}{1 + 4\frac{l_{Du}}{d}} + \frac{2}{\alpha d + \beta l_{Du}} \right]^{-1} \quad (1)$$

where κ_b is the bulk conductivity, L is the pore length, d is the pore diameter, l_{Du} is the Dukhin length (which can be approximated by $\frac{|\Sigma|/e}{2c_s}$, where e is the elementary charge and c_s is the salt concentration), α is a geometrical prefactor that depends on the model used (here, $\alpha = 2$)[19], and β can also be approximated to be 2 to obtain the best fitting agreement[19]. From the fitting results shown in Fig. 2b, we find a surface charge value of $-0.024\ \mathrm{C\,m^{-2}}$, $-0.053\ \mathrm{C\,m^{-2}}$ and $-0.088\ \mathrm{C\,m^{-2}}$ for pores of size 2 nm, 6 nm and 25 nm, respectively, at pH 5. These values are comparable to those reported recently for graphene nanopores ($-0.039\ \mathrm{C\,m^{-2}}$)[20] and nanotubes ($-0.025\ \mathrm{C\,m^{-2}}$ to $-0.125\ \mathrm{C\,m^{-2}}$)[5] at pH 5. The surface charge density can be further modulated by adjusting the pH to change the pore surface chemistry (Fig. 2c). The conductance increases with an increase in pH, suggesting the accumulation of more negative surface charges in MoS₂ nanopores. The simulated conductance from equation (1) at 10 mM KCl is linearly proportional to the surface charge values; thus, pH changes could substantially improve the surface charge up to 0.3–$0.8\ \mathrm{C\,m^{-2}}$. The chemical reactivity of MoS₂ to pH is also supported by measurements of zeta potential on MoS₂ (ref. 21). However we also notice that, as with other nanofluidic systems[5,20], the surface charge density varies from pore to pore, which means that different pores can have disparate values of the equilibrium constant, owing to the various combinations of Mo and S atoms[14] at the edge of the pores (as illuminated by molecular-dynamics simulations[7]).

Next, we introduced a chemical potential gradient by using the KCl concentration gradient system[5]. The concentration gradient ratio is defined as C_{cis}/C_{trans}, where C_{cis} is the KCl concentration in the *cis* chamber and C_{trans} is that in the *trans* chamber; the concentration

ranges from 1 mM to 1 M. The highly negatively charged surface selectively passes the ions (in this case potassium ions) according to their polarity, resulting in a net positive current. By measuring the I–V response of the pore in the concentration gradient system (Fig. 3a), we can measure the short-circuit (I_{sc}) current corresponding to zero external bias, while the osmotic potential can be obtained from the open-circuit voltage (V_{oc}). The pure osmotic potential, V_{os}, and current, I_{os}, can then be obtained by subtracting the contribution from the electrode–solution interface at different concentrations; this contribution follows the Nernst equation[5,22] (Extended Data Fig. 1). The osmotic potential is proportional to the concentration gradient ratio (Fig. 3b) and shares a similar trend with the osmotic current (Fig. 3c).
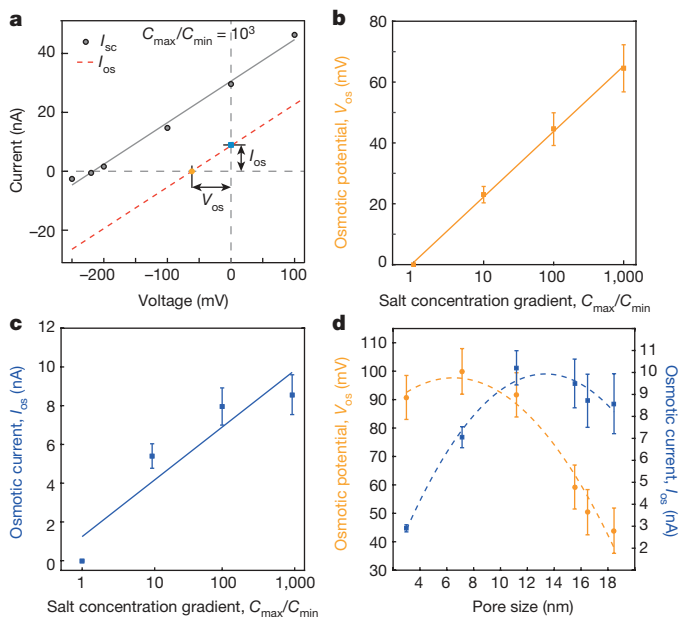

Figure 3 | Osmotic power generation. a, Current–voltage characteristics for a 15-nm nanopore in a 1 M/1 mM KCl gradient. The contribution from the redox reaction on the electrodes is subtracted from the measured total current (grey line) (Extended Data Fig. 1), producing the red dashed line, which represents the pure osmotic contribution. I_{sc} and V_{oc} are the short-circuit current and open-circuit voltage, respectively; I_{os} and V_{os} are the osmotic current and potential. **b**, The generated osmotic potential as a function of the salt gradient. C_{cis} is set to be 1 M KCl; C_{trans} is tunable from 1 mM to 1 M KCl. The solid line represents a linear fitting to equation (2). **c**, Osmotic current as a function of salt gradient. The solid line fits proportionally to the linear part of equation (2). **d**, Osmotic potential and current as a function of pore size. The dashed lines are a guide to the eye and show the trend as the pore size is changed. The error bars come from the corresponding error estimations and represent the s.e.m. (Methods).
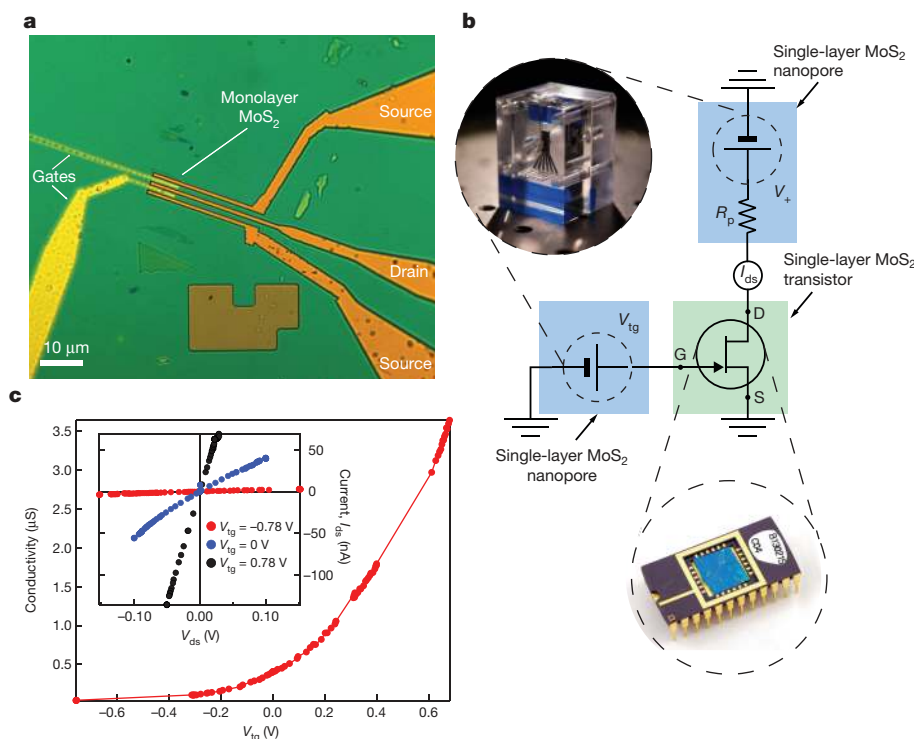
Figure 4 | Demonstration of a self-powered nanosystem. a, Optical image of the fabricated MoS_2 transistor, with a designed gate, and drain and source electrodes. **b**, Circuit diagram for the self-powered nanosystem: the drain–source supply for the MoS_2 transistor is provided by a MoS_2 nanopore, while a second nanopore device operates as the gate voltage source. D, drain; G, gate; S, source; R_p, pore resistance; V_{tg}, gate voltage; V_+, nanopore output voltage. R_p connected in series with V_{tg} has been omitted. **c**, Powering all the terminals of the transistor with nanopore generators. The graph shows the modulated conductivity of the MoS_2 transistor as a function of the top gate voltage (V_{tg}). Inset, current–voltage characteristics at various gate voltages (-0.78 V, 0 V and 0.78 V).

The measured osmotic energy conversion is also pH dependent (Extended Data Fig. 2a, b). The increase in pH leads to higher generated voltage and current, suggesting the importance of surface charge to the ion-selective process.

The extracted osmotic potential is the diffusion potential and it arises from differences in the diffusive fluxes of positive and negative ions, because the pore is ion selective: cations diffuse more rapidly than anions (Fig. 1). The diffusion potential, V_{diff}, can be described as[22]:

$$V_{diff} = S(\Sigma)_{is} \frac{RT}{F} \ln \left[\frac{a_{KCl}^{cis}}{a_{KCl}^{trans}} \right] \qquad (2)$$

Here, $S(\Sigma)_{is}$ is the ion selectivity[23] for the MoS_2 nanopore (and equals 1 for the ideal cation-selective case, and 0 for the non-selective case); it is defined as $S(\Sigma)_{is} = t_+ - t_-$, where t_+ and t_- are the transference numbers for positively and negatively charged ions respectively. F, R and T are the Faraday constant, the universal gas constant, and the temperature, respectively, while a_{KCl}^{cis} and a_{KCl}^{trans} are the activities of potassium ions in *cis* and *trans* solutions. By fitting the experimental data presented in Fig. 3b to equation (2), we find the ion-selectivity coefficient $S(\Sigma)_{is}$ to be 0.4, suggesting efficient cation selectivity. This is because the size of our nanopores lies in the range in which the electrical double-layer overlap can occur inside the pore[18], because the Debye length, λ_B, is 10 nm for 1 mM KCl. As shown in Extended Data Fig. 3d, with a concentration gradient of 10 mM/1 mM in a 5-nm pore, the ion selectivity approaches nearly 1, presenting the conditions for ideal cation selectivity[23].

To test the cation-selective behaviour of the pore further, we investigated the relationship between power generation and pore size. As shown in Fig. 3d, small pores display better voltage behaviour, reflecting better performance in terms of ion selectivity. The ion selectivity, $S(\Sigma)_{is}$, decreases from 0.62 to 0.23 as the pore size increases. We calculated the distribution of surface potential for different pore sizes (2 nm, 5 nm and 25 nm) in order to compare the selectivity difference (Extended Data Fig. 3a–c). It has been proven that the net diffusion current stems only from the charge separation and concentration distribution within the electrical double layer[24], and therefore the total current can be expected to increase more rapidly within small pores

in the double-layer overlap range compared with larger pore sizes (Fig. 3d). This slight decrease in current in larger pores might be attributed to a reduced local concentration gradient, and also to probable overestimation of the redox potential subtraction. The current can be calculated using either a continuum-based Poisson–Nernst–Planck (PNP) model or molecular-dynamics simulations. The measured dependence of the osmotic potential and osmotic current as a function of the concentration ratio (Fig. 3b, c) is well captured by both computational methods (molecular dynamics, Extended Data Fig. 4, and continuum analysis, Extended Data Fig. 5a). The non-monotonic response to pore size (Fig. 3d and Extended Data Fig. 2c, d) might not only be explained by a possible depletion of the local concentration gradient in large pores, but is also predicted by the continuum-based PNP model (Extended Data Fig. 5b) because of the decrease in ion selectivity.

In order to gain further insight into the thickness scaling, we first verified the pore-conductance relation proposed in equation (1) by using molecular dynamics (Extended Data Fig. 6). We found that ion mobility also scales inversely with membrane thickness (Extended Data Fig. 7a, b), which may conform to previous observations[25]. We then performed molecular-dynamics simulations of multilayer membranes of MoS_2 to investigate the power generated by those membranes. We observe a strong decay in the generated power as the number of layers increases (Extended Data Fig. 7c, d), indicating that the best osmotic power generation occurs in two-dimensional membranes. The consistency between experiments and theoretical models highlights two important factors in achieving efficient power generation from a single-layer MoS_2 nanopore: atomic-scale pore thickness and surface charge.

If we have a single-layer MoS_2 membrane with a homogeneous pore size of 10 nm and a porosity of 30%, then, by exploiting parallelization, the estimated power density would reach 10^6 W m^{-2} with a KCl salt gradient. These values exceed—by two to three orders of magnitude— the results obtained with boron nitride nanotubes[5], and are a million times higher than the power density obtained by reverse electrodialysis with classical exchange membranes[1] (Extended Data Table 1).

As well as using KCl concentration gradients, the nanopore power generator concept could also be applied to liquid–liquid junction

systems with a chemical potential gradient, because the diffusion voltage originates from the Gibbs mixing energy of the two liquids (Supplementary Information). Thus, high-performance, nanopore-based generators based on a large number of available liquid combinations could be explored[24]. For example, we have shown substantial power generation based on a chemical potential gradient that uses two types of liquid (Extended Data Fig. 8d). Considerable energy could also be generated by exploiting parallelization, with multiple small pores or even a continuous porous structure within a large area of single-layer MoS₂ membrane[26], which could be scaled up for mass production using the ECR pore-fabrication technique[16] or plasma-based defect creation[27].

The use of individual nanopores as a micro/nano power source has long been expected[22]. We find here that an individual osmotic generator can also serve as a nanopower source for a self-powered nanosystem, owing to its high efficiency and power density. For this self-powered nanosystem, we chose the high-performance single-layer MoS₂ transistor (Fig. 4a) because of its excellent operation at low power[28]. We characterized this transistor in the configuration shown in Fig. 4b, using two nanopores to apply voltages to the transistor's drain and gate terminals. As shown in Fig. 4c, by varying the top gate voltage in the relatively narrow window of ±0.78 V, we could modulate the channel conductivity by a factor of 50 to 80. Furthermore, when we fixed the gate voltage and varied the drain–source voltage V_{ds}, (Fig. 4c inset), we obtained a linear I_{ds}–V_{ds} curve, demonstrating efficient injection of electrons into the transistor channel. Further calibration with a standard power source can be found in Extended Data Fig. 8. This system is an ideal self-powered nanosystem in which all the devices are based on single-layer MoS₂.

We have shown that MoS₂ nanopores are promising candidates for investigating osmotic power generation as a renewable energy source. The substantial power generated in our experiments can be attributed mainly to the atomic-scale thickness of the MoS₂ membrane. Our results also provide new avenues for studying other membrane-based processes, such as water desalination[7] or proton transport[29]. Furthermore, the nanopore generator may see application in other ultralow-power devices, such as in electronics.

Online Content Methods, along with any additional Extended Data display items and Source Data, are available in the online version of the paper; references unique to these sections appear only in the online paper.

1. Logan, B. E. & Elimelech, M. Membrane-based processes for sustainable power generation using water. *Nature* **488**, 313–319 (2012).
2. Pattle, R. Production of electric power by mixing fresh and salt water in the hydroelectric pile. *Nature* **174**, 660 (1954).
3. Loeb, S. Osmotic power-plants. *Science* **189**, 654–655 (1975).
4. van der Heyden, F. H., Stein, D. & Dekker, C. Streaming currents in a single nanofluidic channel. *Phys. Rev. Lett.* **95**, 116104 (2005).
5. Siria, A. *et al.* Giant osmotic energy conversion measured in a single transmembrane boron nitride nanotube. *Nature* **494**, 455–458 (2013).
6. Suk, M. E. & Aluru, N. Water transport through ultrathin graphene. *J. Phys. Chem. Lett.* **1**, 1590–1594 (2010).
7. Heirarian, M., Farimani, A. B. & Aluru, N. R. Water desalination with a single-layer MoS₂ nanopore. *Nature Commun.* **6**, 8616 (2015).
8. Wang, Z. L. & Song, J. Piezoelectric nanogenerators based on zinc oxide nanowire arrays. *Science* **312**, 242–246 (2006).
9. Wang, Z. L. Self-powered nanosensors and nanosystems. *Adv. Mater.* **24**, 280–285 (2012).
10. Tian, B. *et al.* Coaxial silicon nanowires as solar cells and nanoelectronic power sources. *Nature* **449**, 885–889 (2007).
11. Xu, S. *et al.* Self-powered nanowire devices. *Nature Nanotechnol.* **5**, 366–373 (2010).
12. Wu, W. *et al.* Piezoelectricity of single-atomic-layer MoS₂ for energy conversion and piezotronics. *Nature* **514**, 470–474 (2014).
13. Liu, K., Feng, J., Kis, A. & Radenovic, A. Atomically thin molybdenum disulfide nanopores with high sensitivity for DNA translocation. *ACS Nano* **8**, 2504–2511 (2014).
14. Farimani, A. B., Min, K. & Aluru, N. R. DNA base detection using a single-layer MoS₂. *ACS Nano* **8**, 7914–7922 (2014).
15. Liu, X. *et al.* Top–down fabrication of sub-nanometre semiconducting nanoribbons derived from molybdenum disulfide sheets. *Nature Commun.* **4**, 1776 (2013).
16. Feng, J. *et al.* Electrochemical reaction in single layer MoS₂: nanopores opened atom by atom. *Nano Lett.* **15**, 3431 (2015).
17. Stein, D., Kruithof, M. & Dekker, C. Surface-charge-governed ion transport in nanofluidic channels. *Phys. Rev. Lett.* **93**, 035901 (2004).
18. Bocquet, L. & Charlaix, E. Nanofluidics, from bulk to interfaces. *Chem. Soc. Rev.* **39**, 1073–1095 (2010).
19. Lee, C. *et al.* Large apparent electric size of solid-state nanopores due to spatially extended surface conduction. *Nano Lett.* **12**, 4037–4044 (2012).
20. Shan, Y. *et al.* Surface modification of graphene nanopores for protein translocation. *Nanotechnology* **24**, 495102 (2013).
21. Ge, P. *et al.* Hydrogen evolution across nano-schottky junctions at carbon supported MoS₂ catalysts in biphasic liquid systems. *Chem. Commun.* **48**, 6484–6486 (2012).
22. Kim, D.-K., Duan, C., Chen, Y.-F. & Majumdar, A. Power generation from concentration gradient by reverse electrodialysis in ion-selective nanochannels. *Microfluid. Nanofluidics* **9**, 1215–1224 (2010).
23. Vlassiouk, I., Smirnov, S. & Siwy, Z. Ionic selectivity of single nanochannels. *Nano Lett.* **8**, 1978–1985 (2008).
24. Cao, L. *et al.* Towards understanding the nanofluidic reverse electrodialysis system: well matched charge selectivity and ionic composition. *Energy Environ. Sci.* **4**, 2259–2266 (2011).
25. Wu, J., Gerstandt, K., Zhang, H., Liu, J. & Hinds, B. J. Electrophoretically induced aqueous flow through single-walled carbon nanotube membranes. *Nature Nanotechnol.* **7**, 133–139 (2012).
26. Waduge, P. *et al.* Direct and scalable deposition of atomically thin low-noise MoS₂ membranes on apertures. *ACS Nano* **9**, 7352–7359 (2015).
27. Surwade, S. P. *et al.* Water desalination using nanoporous single-layer graphene. *Nature Nanotechnol.* **10**, 459–464 (2015).
28. Radisavljevic, B., Radenovic, A., Brivio, J., Giacometti, V. & Kis, A. Single-layer MoS₂ transistors. *Nature Nanotechnol.* **6**, 147–150 (2011).
29. Walker, M. I., Braeuninger-Weimer, P., Weatherup, R. S., Hofmann, S. & Keyser, U. F. Measuring the proton selectivity of graphene membranes. *Appl. Phys. Lett.* **107**, 213104 (2015).

Supplementary Information is available in the online version of the paper.

Author Contributions J.F. and A.R. conceived the idea, designed all experiments, and wrote the manuscript. J.F. and M.G. performed measurements and data analysis. J.F. and K.L. fabricated the nanopore device. D.O. fabricated the MoS₂ transistor and D.D. performed chemical-vapour-deposition MoS₂ growth under A.K.'s supervision. J.F. and D.O. demonstrated the self-powering of the nanosystem. M.H., V.N., and N.R.A. built the computational nanofluidics model and interpreted the simulation results. All authors provided constructive comments on the manuscript.

Author Information Reprints and permissions information is available at www.nature.com/reprints. The authors declare no competing financial interests. Readers are welcome to comment on the online version of the paper. Correspondence and requests for materials should be addressed to J.F. (jiandong.feng@epfl.ch) or A.R. (aleksandra.radenovic@epfl.ch).

Reviewer Information *Nature* thanks Z. Siwy and the other anonymous reviewer(s) for their contribution to the peer review of this work.

METHODS

Nanopore fabrication. We fabricated MoS_2 nanopores either by using the atomic-scale ECR technique[16] or by electron irradiation under TEM[13]. Prior to nanopore fabrication, we create a freestanding MoS_2 membrane[30]. Briefly, we use KOH wet etching to prepare SiN_x membranes (of size $10\,\mu m \times 10\,\mu m$ to $50\,\mu m \times 50\,\mu m$; 20 nm thick). We then use focused ion beam (FIB) or ebeam lithography (followed by reactive ion etching) to drill an opening of 50–300 nm in the membrane. Next we suspend single-layer MoS_2 membranes, grown by chemical-vapour deposition, on the opening by transferring them from sapphire growth substrates[30]. TEM irradiation can be applied to drill a single pore and image the pore. ECR is done by applying a step-like transmembrane potential to the membrane and monitoring the transmembrane ionic current with a Femto DLPCA-200 amplifier (Femto Messtechnik GmbH), with a custom-made feedback control on transmembrane conductance. Nanopores are formed when reaching the critical voltage of MoS_2 oxidation (>0.8 V). We then calibrate the pore size using I–V characteristics.

Nanofluidic measurements. Nanofluidic transport experiments are performed as described[16]. The nanopore chips are mounted in a custom-made polymethylmethacrylate chamber, and then wetted with an H_2O:ethanol (1:1) solution. Nanofluidic measurements are carried out by taking the I–V characteristics of the nanopore in different KCl solutions (Sigma Aldrich; the ionic concentration or pH of the solution varies), using an Axopatch 200B patch-clamp amplifier (Molecular Devices Inc.). A pair of chlorinated Ag/AgCl electrodes (which have been rechlorinated regularly) is used to apply voltage and to measure the current. In addition, the electrode potential differences in solutions of different concentrations are calibrated with a saturated Ag/AgCl reference electrode (Sigma Aldrich).

To measure osmotic power generation, we filled the reservoirs with solutions of different concentrations, ranging from 1 mM to 1 M. Measurements are performed at various pH conditions. We found that power generation was optimal at pH 11. First, we measured the I–V response; we obtained the short-circuit current from the interception of the curve at zero voltage, and the open-circuit voltage from the interception of the curve at zero current. Next, to get the purely osmotically driven contribution, we subtracted the contribution made by the electrode potential difference that results from the redox potential in different concentrations (Extended Data Fig. 1).

For all experiments, we performed cross-checking measurements, including changing the direction of pH and concentration to make sure that the nanopores were not substantially enlarged during the experiments. Most MoS_2 pores were generally stable during hours of experiments owing to their high mechanical strength and stability within the ±600 mV bias range. Thus, we strongly recommend the use of small supporting FIB/ebeam-drilled opening windows (of diameter 50–300 nm) for suspended membranes.

Characterization of single-layer MoS_2 transistors. We fabricated single-layer MoS_2 transistors using a procedure similar to that in ref. 28.

For electrical measurements we used an Agilent 5270B source-meter unit (SMU), an SR-570 low-noise current preamplifier and a Keithley 2000 digital multimeter (DMM; input impedance >$10^{10}\,\Omega$). All measurements were performed in ambient conditions in the dark. An improved efficiency of power conversion in nanopores is obtained by using a combination of pure room-temperature ionic liquids: 1-butyl-2-methylimidazolium hexafluorophosphate (Bmim PF_6) and zinc chloride solution.

We compare the performance of the single-layer MoS_2 transistor in two cases. First, we use two nanopores to apply V_{tg} and V_{ds}, while using a current amplifier and voltmeter to control the current and voltage drop across the device (see Extended Data Fig. 8a). In this case, we use voltage dividers to change the source and gate voltage on the device (not shown in Fig. 4a and Extended Data Fig. 8a). Second, we use the SMU to perform standard two-contact measurements.

Although the characteristics of our transistor are similar in both set-ups, we comment here on the difference detected in the conductivity of the ON state. We attribute it to the slow response of the device in the first case. The change in transistor resistance that occurs when applying gate voltage leads to a change in the impedance of the device and thus a change in the applied effective voltage, V_{dev} (measured with a voltmeter connected in parallel). The nanopore reacts to the change in impedance with a certain stabilization time (from 10 s to 100 s). This appears to be a hysteretic effect and influences the conductivity versus gate-voltage measurements. In the second case, on the other hand, $V_{dev} = V_{ds}$ is constant. There are several secondary effects, which might in turn influence the measured values of two-probe conductivity. In relatively short channel devices, applied V_{ds} might partially contribute to gating of the channel and furthermore to modification of contact resistance. This could be understood by comparing the values of V_{ds} (around 100 mV) and V_{tg} (780 mV). We also do not exclude the possibility of slight doping variations and hysteretic effects that occur because of the filling of trap states inside the transistor channel. However, by driving a device to the ON state and stabilizing the current for a reasonable amount of

time, we obtained a very good match in drain–source I_{ds}–V_{ds} characteristics (Extended Data Fig. 8c). We thus conclude that, although there are differences in performance in the two cases, these differences originate mainly from the slow response time of the nanopore.

We extracted the resistance and power of the nanopore by using the ionic liquid Bmim PF_6. By considering the simple resistor network (Extended Data Fig. 8d, inset), we could extract the output power as a function of the load resistance, R_{load}. We fit our dependence according to the following model, which assumes a constant V_{out} and R_{pore}:

$$\text{Power} = \frac{V_{out} R_{load}}{(R_p + R_{load})^2}$$

and found a good fit with $V_{out} = 0.83$ V, which is close to the measured V_{out} of 0.78 V, and with a nanopore impedance, R_p, of $9.4 \pm 2.1\,M\Omega$ (Extended Data Fig. 8d).

Data analysis. All data analysis has been done using custom-made Matlab (R2016a) code. First, we recorded I–V characteristics with an Axopatch 200B amplifier, by using either an automatic or a manual voltage switch. We then segmented the current trace into pieces of constant voltage, V. We extracted the mean, $\mu(V)$, and standard deviation, $\sigma(V)$, of the stable part of each segment and generated an I–V plot. The error bars are the standard deviations (see Fig. 3 and Extended Data Fig. 2). All I–V characteristics were linear. In order to propagate the error correctly, we used a linear fitting method[31]. Using this method, we can extract the a, b, σ_a and σ_b values of the first-order polynomial $I(V) = b\,V + a$. The conductance is the slope, b, of the I–V curve, and a describes the offset. The height of the error bars reported for conductance measurements is $2\sigma_b$.

We report the osmotic power generation using the osmotic current, I_{os}, and osmotic voltage, V_{os}. Starting from the linear-fit values of the I–V plot, we can calculate the measured current and voltage: $I_{meas} = a$ and $V_{meas} = a/b$. These measured values have to be adjusted for the electrode potential: $V_{os} = V_{meas} - V_{redox}$ and $I_{os} = (V_{os}/V_{meas}) \times I_{meas}$. Assuming an uncertainty in our estimation of redox potential, σ_{redox}, of 5%, we can propagate the errors using the following formulas[32]:

$$\sigma_{V_{os}} = \sqrt{\left(\frac{1}{b}\sigma_a\right)^2 + \left(\frac{a}{b^2}\sigma_b\right)^2 + \sigma_{redox}^2}$$

$$\sigma_{I_{os}} = \sqrt{\sigma_a^2 + (V_{redox}\sigma_b)^2 + b^2\sigma_{redox}^2}$$

We used these relations to calculate the error bars shown in plots of osmotic voltage and current (Fig. 3 and Extended Data Fig. 2).

Computational simulations. *Molecular-dynamics simulations.* These simulations were performed using the LAMMPS package[33]. A MoS_2 membrane was placed between two KCl solutions as shown in Extended Data Fig. 4a. A fixed graphene wall was placed at the end of each solution reservoir. A nanopore was drilled in MoS_2 by removing the desired atoms. The accessible pore diameter considered in all of the molecular-dynamics simulations is 2.2 nm with a surface charge density of $-0.04694\,C\,m^{-2}$. The system dimensions were $6\,nm \times 6\,nm \times 36\,nm$ in the x, y and z directions, respectively. We used the extended simple point charge (SPC/E) water model, and applied the SHAKE algorithm to maintain the rigidity of each water molecule. The Lennard Jones (LJ) parameters are tabulated in Supplementary Table 1. The LJ cut-off distance was 12 Å. The long-range interactions were computed by the particle–particle particle–mesh (PPPM) method[34]. Periodic boundary conditions were applied in the x and y directions. The system is non-periodic in the z direction. For each simulation, first the energy of the system was minimized for 10,000 steps. Next, the system was equilibrated in the isothermic–isobaric (otherwise known as NPT) ensemble for 2 ns at a pressure of 1 atm and a temperature of 300 K to reach the equilibrium density of water. Graphene and MoS_2 atoms were held fixed in space during the simulations. Then, canonical (NVT) simulations were performed, during which the temperature was maintained at 300 K by using the Nosè–Hoover thermostat with a time constant of 0.1 ps (refs 35, 36). Trajectories of atoms were collected every picosecond to obtain the results. For accurate mobility calculations, however, the trajectories were stored every ten femtoseconds.

Continuum model. We also used the continuum-based two-dimensional Poisson–Nernst–Planck (PNP) model. We neglected the contribution of H^+ and OH^- ions in this calculation, as their concentrations are much lower compared with the bulk concentration of the other ionic species (K^+ and Cl^-). Hence, water-dissociation effects are not considered in the numerical model. Further, we assumed that the ions are immobile inside the steric layer and do not contribute to the ionic current. We also did not model the Faradaic reactions occurring near the electrode. Finally, we assumed that the convective component of current originating from the fluid flow is negligible and does not contribute to the non-monotonic osmotic current observed in our experiments. We validated this assumption by performing detailed

all-atom molecular-dynamics simulations and predicted the contribution of electroosmotic velocity in comparison with the drift velocity of the ions.

Under these assumptions, the total flux of each ionic species ($\boldsymbol{\Gamma_i}$) is contributed by a diffusive component resulting from the concentration gradient, and an electrophoretic component arising from the potential gradient, as given by:

$$\boldsymbol{\Gamma_i} = -D_i \boldsymbol{\nabla} c_i - \Omega_i z_i F c_i \boldsymbol{\nabla} \phi$$

where F is Faraday's constant, z_i is the valence of the ith species, D_i is the diffusion coefficient, Ω_i is the ionic mobility, c_i is the concentration and ϕ is the electrical potential. Note that the ionic mobility is related to the diffusion coefficient by Einstein's relation[37], $\Omega_i = \frac{D_i}{RT}$, where R is the ideal gas constant and T is the thermodynamic temperature. The mass transport of each ionic species is:

$$\frac{dc_i}{dt} = -\boldsymbol{\nabla} \cdot \boldsymbol{\Gamma_i}$$

The individual ionic current (I_i) across the reservoir and the pore is calculated by integrating their respective fluxes over the cross-sectional area, that is:

$$I_i = \int z_i F \boldsymbol{\Gamma_i} dS$$

The total ionic current at any axial location is calculated as $I = \sum_{i=1}^{m} z_i F \boldsymbol{\Gamma_i} dS$, where S is the cross-sectional area corresponding to the axial location and m is the number of ionic species. In order to determine the electric potential along the system, we solve the Poisson equation:

$$\boldsymbol{\nabla} \cdot (\epsilon_r \boldsymbol{\nabla} \phi) = -\frac{\rho_e}{\epsilon_0}$$

where ϵ_0 is the permittivity of free space, ϵ_r is the relative permittivity of the medium and ρ_e is the net space charge density of the ions, defined as:

$$\rho_e = F \sum_{i=1}^{m} z_i c_i$$

We provide the necessary boundary conditions for the closure of the problem. The normal flux of each ion is assumed to be zero on all the walls so that there is no leakage of current. To conserve charge on the walls of the pore, the electrostatic boundary condition is given by:

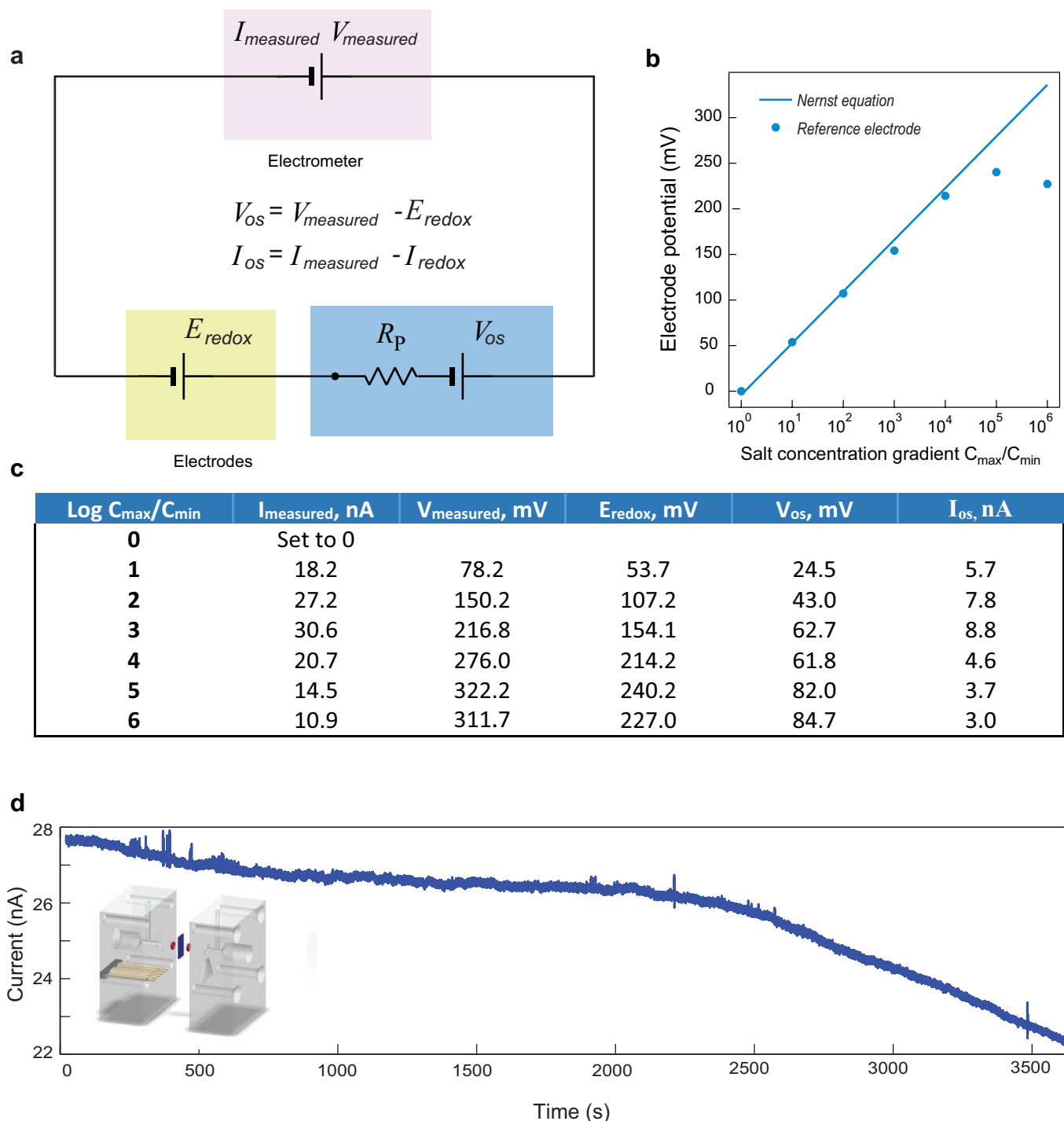$$\boldsymbol{n} \cdot \boldsymbol{\nabla} \phi = \frac{\sigma}{\epsilon_0 \epsilon_r}$$

where $\boldsymbol{n}$ denotes the unit normal vector (pointing outwards) to the wall surface and σ is the surface charge density of the walls. The bulk concentration of the *cis* reservoir is maintained at C_{max} and the bulk concentration on the *trans* reservoir is maintained at C_{min}. As we are interested in understanding the osmotic short-circuit current, I_{sc}, we do not apply any voltage difference across the reservoirs. Thus, the boundary conditions at the ends of the *cis* and *trans* reservoirs are specified as:

$$c_i = C_{max}, \phi = 0$$

$$c_i = C_{min}, \phi = 0$$

The coupled PNP equations are numerically solved using the finite volume method in OpenFOAM (http://www.openfoam.com/). The details of solver implementation are discussed in refs 38–40. The simulated domain consisted of a MoS_2 nanopore of length, L_n, 0.6 nm and diameter, d_n, varying from 2.2 nm to 25 nm. The simulated length of the reservoir was $L_{cis} = L_{trans} = 11$ nm; the diameter of the reservoir was 50 nm. KCl buffer solution was used in the simulation. The bulk concentration of the *cis* reservoir was fixed at 1 M and the concentration in the *trans* reservoir was varied systematically varied from 1 mM to 1 M. The simulation temperature was 300 K. The bulk diffusivities of K^+ and Cl^- were 1.96×10^{-9} m^2 s^{-1} and 2.03×10^{-9} m^2 s^{-1}. The dielectric constant of the aqueous solution was assumed to be 80. We also assumed zero surface charge density on the walls of the reservoir, as the reservoir is too far away from the nanopore to have an influence on the transport. Unless otherwise stated, the charge on the walls of the MoS_2 nanopore is assumed to be $\sigma_n = -0.04694$ C m^{-2}, consistent with the surface charge calculated from our molecular-dynamics simulations.

30. Dumcenco, D. *et al.* Large-area epitaxial monolayer MoS₂. *ACS Nano* **9**, 4611–4620 (2015).
31. York, D., Evensen, N. M., Martınez, M. L. & Delgado, J. D. B. Unified equations for the slope, intercept, and standard errors of the best straight line. *Am. J. Phys.* **72**, 367–375 (2004).
32. Ku, H. Notes on the use of propagation of error formulas. *J. Res. National Bureau Standards* **70C**, 263–273 (1966).
33. Plimpton, S. Fast parallel algorithms for short-range molecular dynamics. *J. Comput. Phys.* **117**, 1–19 (1995).
34. Hockney, R. W. & Eastwood, J. W. *Computer Simulation Using Particles* (CRC Press, 1988).
35. Nosé, S. A unified formulation of the constant temperature molecular dynamics methods. *J. Chem. Phys.* **81**, 511–519 (1984).
36. Hoover, W. G. Canonical dynamics: equilibrium phase-space distributions. *Phys. Rev. A* **31**, 1695–1697 (1985).
37. Probstein, R. F. *Physicochemical Hydrodynamics: An Introduction.* (John Wiley & Sons, 2005).
38. Nandigana, V. V. & Aluru, N. Understanding anomalous current–voltage characteristics in microchannel–nanochannel interconnect devices. *J. Colloid Interface Sci.* **384**, 162–171 (2012).
39. Nandigana, V. V. & Aluru, N. Nonlinear electrokinetic transport under combined ac and dc fields in micro/nanofluidic interface devices. *J. Fluids Eng.* **135**, 021201 (2013).
40. Nandigana, V. V. & Aluru, N. Characterization of electrochemical properties of a micro–nanochannel integrated system using computational impedance spectroscopy (cis). *Electrochim. Acta* **105**, 514–523 (2013).
41. Weinstein, J. N. & Leitz, F. B. Electric power from differences in salinity: the dialytic battery. *Science* **191**, 557–559 (1976).
42. Audinos, R. Reverse electrodialysis. Study of the electric energy obtained by mixing two solutions of different salinity. *J. Power Sources* **10**, 203–217 (1983).
43. Turek, M. & Bandura, B. Renewable energy by reverse electrodialysis. *Desalination* **205**, 67–74 (2007).
44. Suda, F., Matsuo, T. & Ushioda, D. Transient changes in the power output from the concentration difference cell (dialytic battery) between seawater and river water. *Energy* **32**, 165–173 (2007).
45. Veerman, J., De Jong, R., Saakes, M., Metz, S. & Harmsen, G. Reverse electrodialysis: comparison of six commercial membrane pairs on the thermodynamic efficiency and power density. *J. Membr. Sci.* **343**, 7–15 (2009).

a

$$I_{measured} \quad V_{measured}$$

Electrometer

$$V_{os} = V_{measured} - E_{redox}$$
$$I_{os} = I_{measured} - I_{redox}$$

$$E_{redox} \qquad R_P \qquad V_{os}$$

Electrodes

b

c

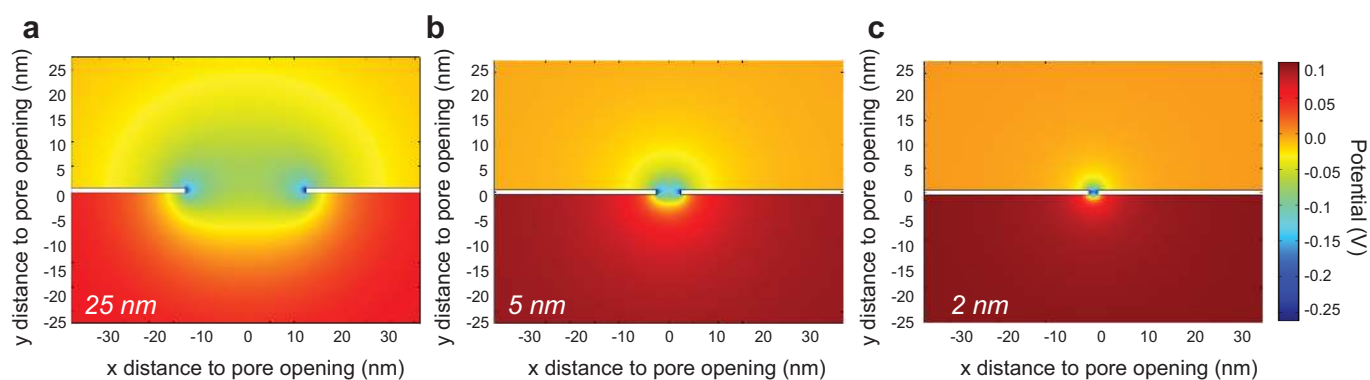| Log C_{max}/C_{min}	$I_{measured}$, nA	$V_{measured}$, mV	E_{redox}, mV	V_{os}, mV	I_{os}, nA
0	Set to 0				
1	18.2	78.2	53.7	24.5	5.7
2	27.2	150.2	107.2	43.0	7.8
3	30.6	216.8	154.1	62.7	8.8
4	20.7	276.0	214.2	61.8	4.6
5	14.5	322.2	240.2	82.0	3.7
6	10.9	311.7	227.0	84.7	3.0

d

Extended Data Figure 1 | Subtraction of the contribution made by electrodes, and stability of the nanopore generator. a, Diagram showing the contributions of different parts of the system to the overall measured current. The osmotic contribution is obtained by subtracting the contribution of the potential difference at the electrodes from the measured voltage or current. $V_{measured}$ is the measured voltage; E_{redox} is the redox potential difference. **b**, Electrode contribution as a function of the salt concentration gradient: values obtained from the Nernst equation, and measured electrode redox potential differences at the reference electrode. **c**, The data used for the subtraction. E_{redox}, the redox potential at the electrodes. **d**, A 1-hour trace of ionic current, showing the stability of a 14-nm pore in 1 M KCl/1 mM KCl. Inset, the design of the fluidic cell.
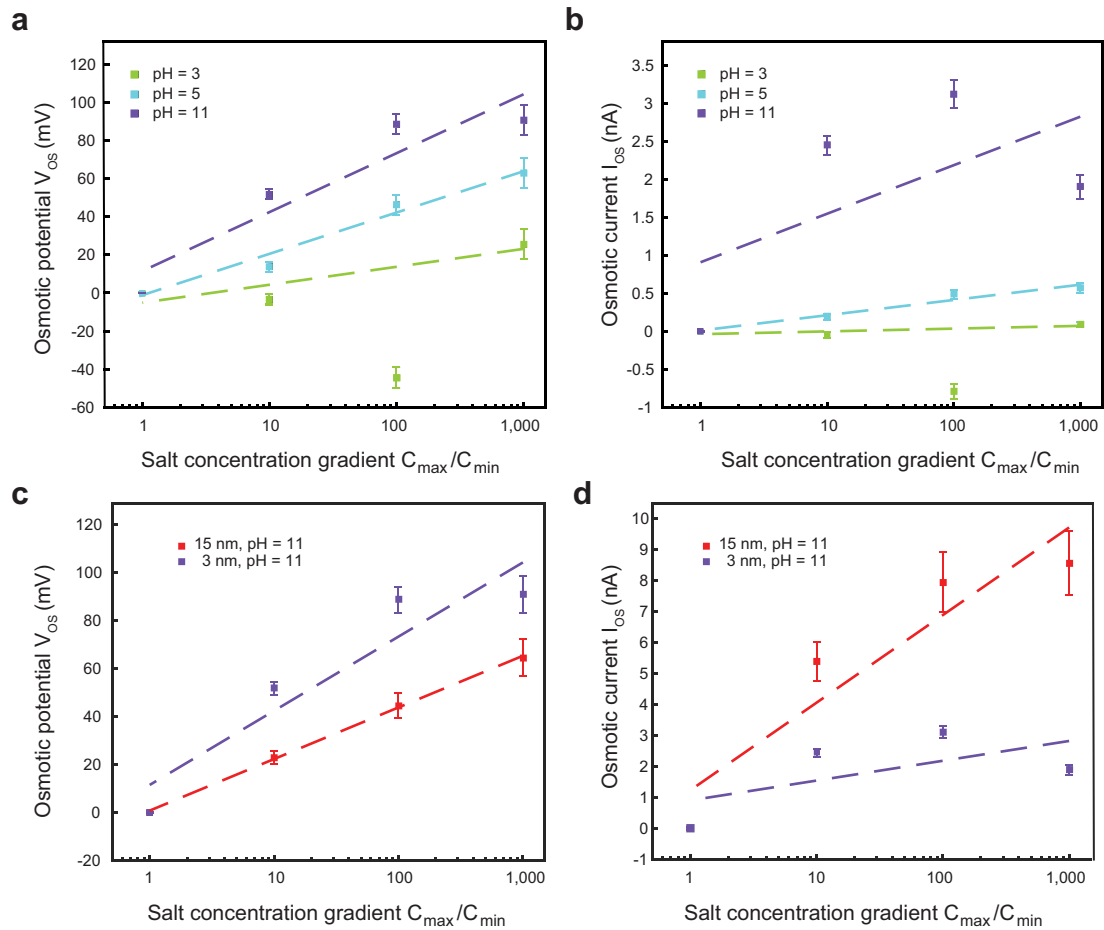
Extended Data Figure 2 | Dependence of osmotic power generation on pH and pore size. a, b, Osmotic potential (**a**) and osmotic current (**b**) generated using a 3-nm pore under different pH conditions (pH 3, 5 or 11) and in different concentration gradients. Power generation (both osmotic potential and osmotic cu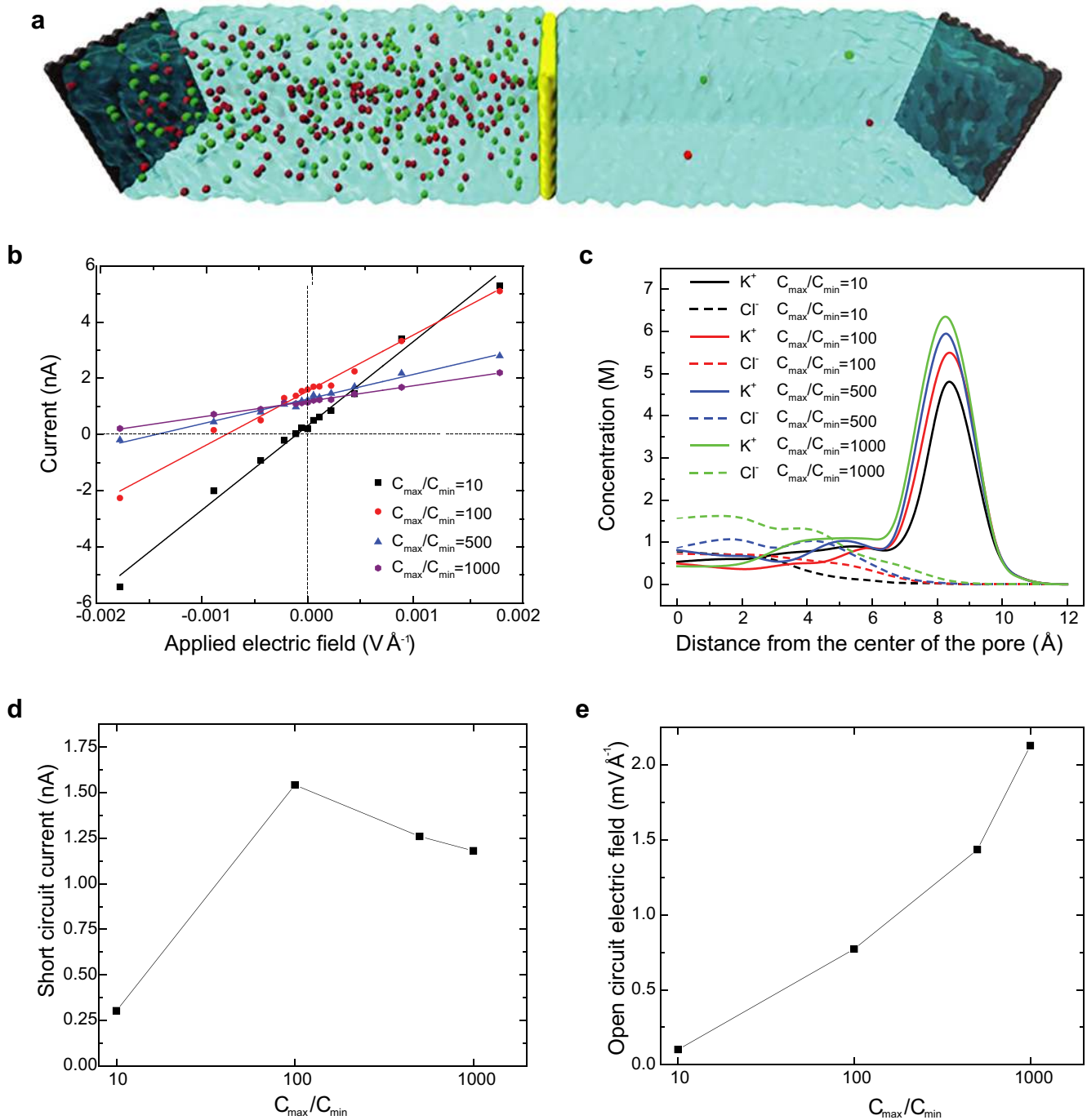rrent) at pH 3 is very low and sometimes fluctuates to negative, indicating that the pore charge is relatively low. One possible explanation for the negative voltage point is that the surface charge on the pore has fluctuated to positive. **c, d**, Osmotic potential (**c**) and osmotic current (**d**) generated using two different pores (3-nm and 15-nm) at pH 11 in different concentration gradients.

Extended Data Figure 3 | Ideal cation selectivity of the pore.
a–c, Calculated surface potential distribution of MoS_2 nanopores of diameter 25 nm (**a**), 5 nm (**b**), and 2 nm (**c**) under a fixed surface charge density. **d**, Ion selectivity in different salt gradients. The ion selectivity also depends on the Debye length when the concentration gradient is fixed; with a gradient of 10 mM/1 mM and a 5-nm pore, the ion selectivity approaches nearly 1, indicating the ideal cation selectivity.

d

| C_{min}/C_{max}	$V_{measured}$, mV	E_{redox}, mV	V_{os}, mV	Ion selectivity
1mM/10mM	100.6	46.9	53.7	0.92
10mM/100mM	104.4	53.5	50.9	0.86
10mM/1M	153.3	107.2	46.1	0.78
1mM/100mM	183.0	100.4	82.6	0.7
100mM/1M	67.3	53.7	13.6	0.23

Extended Data Figure 4 | Molecular-dynamics simulations of power generation for various ratios of concentration gradients. a, A typical simulation box. **b**, Current as a function of the applied electric field for a single-layer MoS_2, at different concentration ratios. **c**, K^+ and Cl^- concentrations as a function of the radial distance from the centre of the pore, for different concentration ratios. **d**, Short-circuit current as a function of the concentration ratio. **e**, Open-circuit electric field as a function of the concentration ratio.
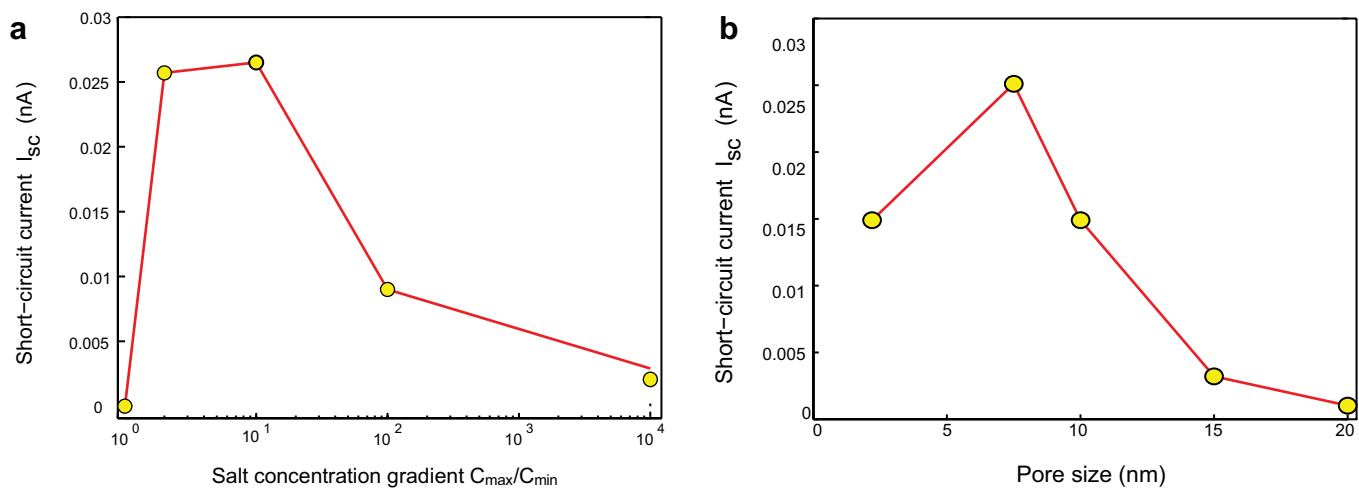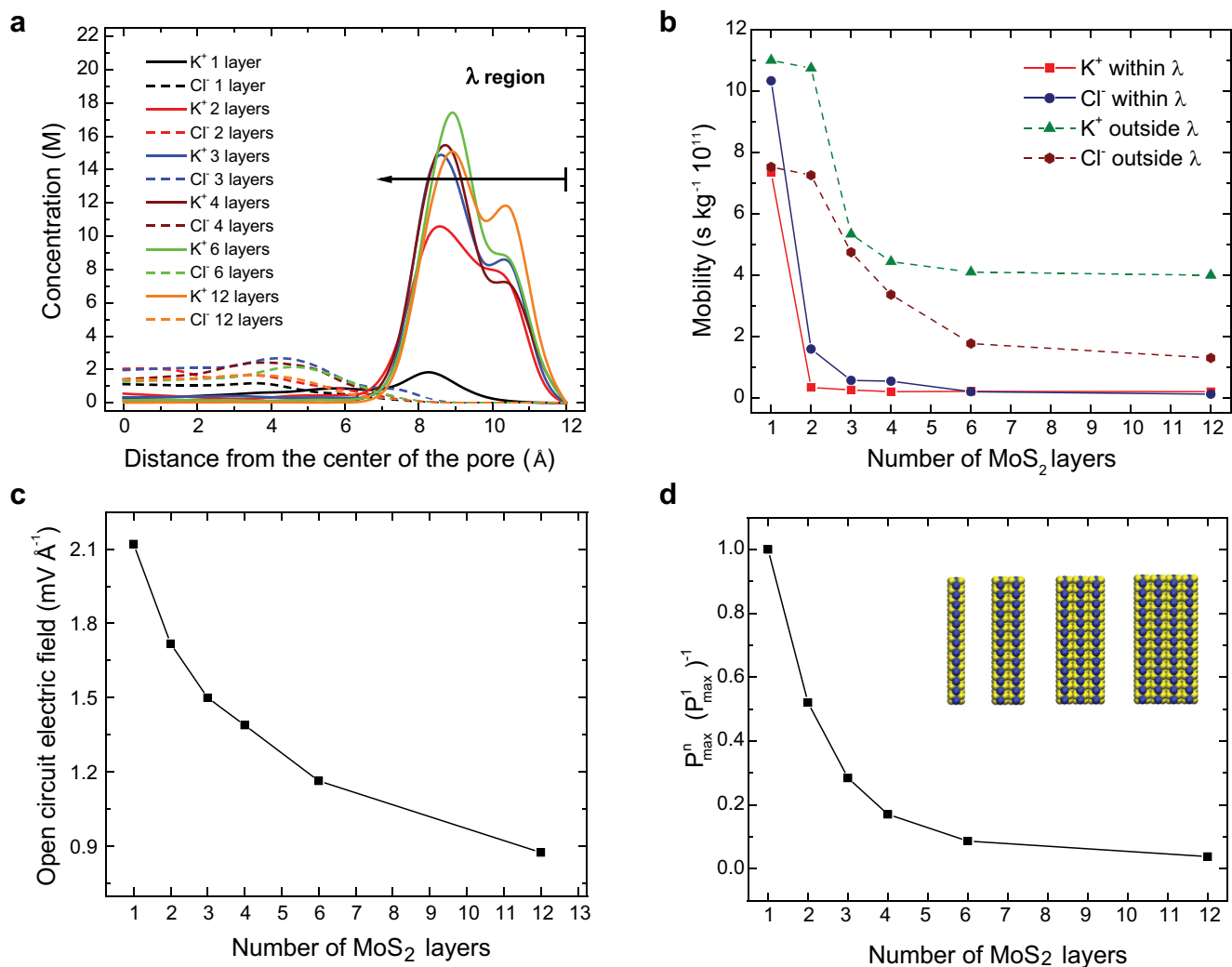
Extended Data Figure 5 | Continuum-based PNP modelling of power generation. a, Short-circuit current, I_{sc}, as a function of the concentration gradient ratio. The diameter of the nanopore here is 2.2 nm. **b**, I_{sc} as a function of the nanopore diameter. The salinity concentration ratio is fixed at 1,000. The surface charge of the nanopore, σ_n, is $-0.04694\,C\,m^{-2}$.
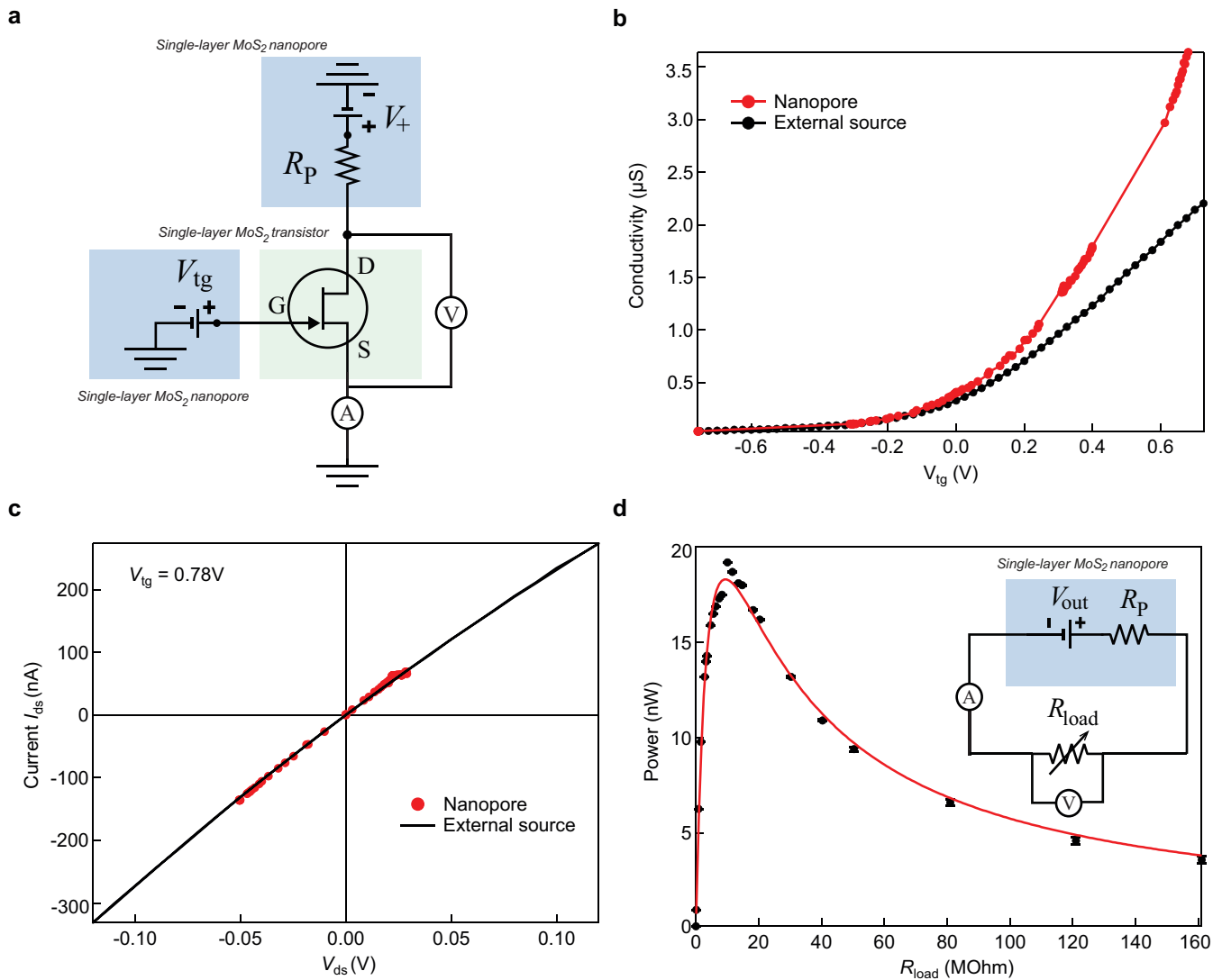
a

b

c
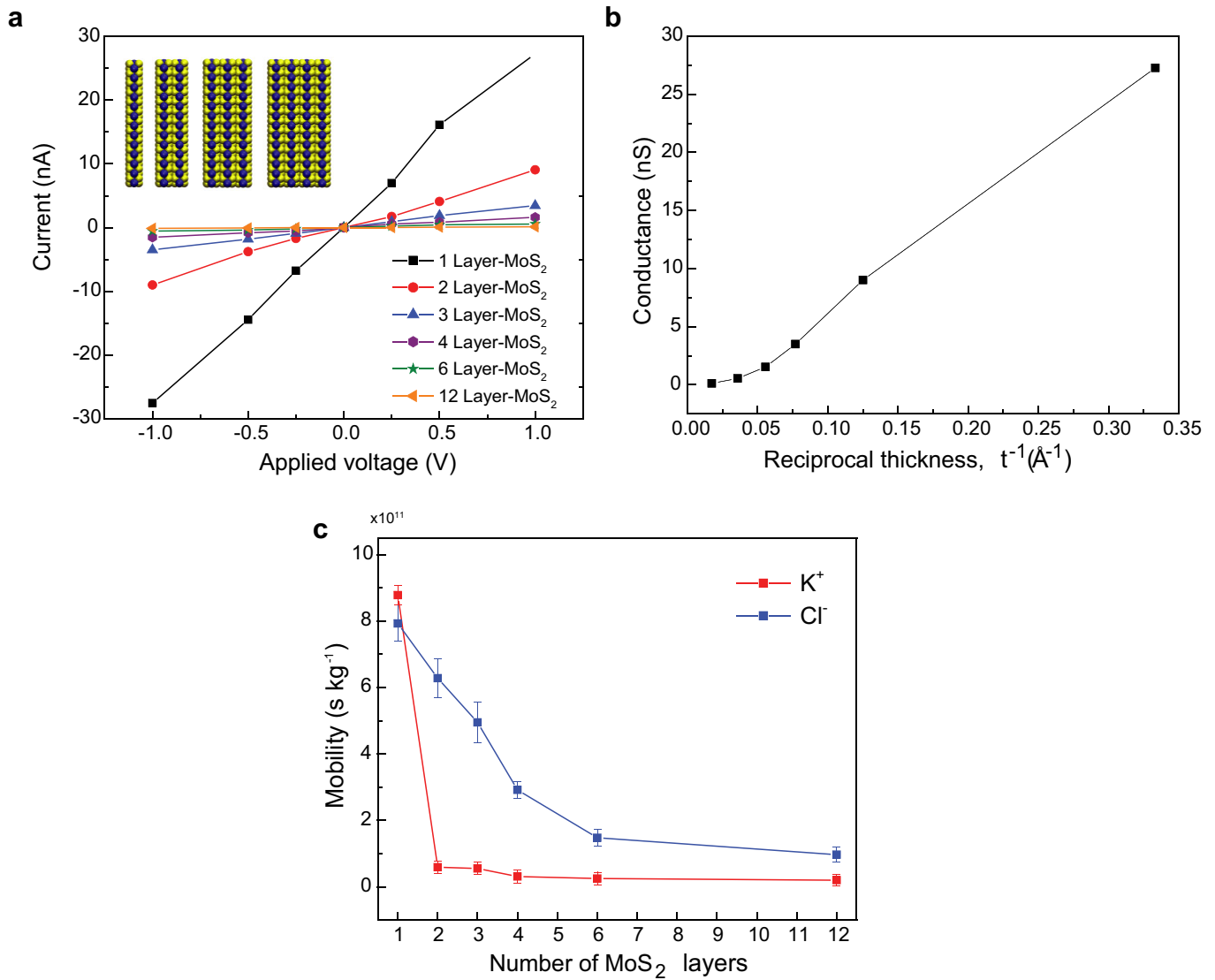
Extended Data Figure 6 | Molecular-dynamics-modelled conductance as a function of membrane thickness. a, I–V curves for six membranes with a different number of MoS_2 layers, across a symmetrical 1 M KCl solution. The inset illustrates simulated multilayer membranes. **b**, Conductance of the nanopore as a function of the reciprocal thickness of the membrane (t^{-1}). **c**, Average mobility of each ion for different numbers of layers of MoS_2 membranes.

a, K$^+$ and Cl$^-$ concentrations as a function of the radial distance from the centre of the pore for single-layer and multilayer membranes. The λ region, near the charged wall of the pore, is representative of the electrical double layer. **b**, The mobility of each ion type within and outside the λ region for different layers of membranes. **c**, The open-circuit electric field across the membrane for different numbers of MoS$_2$ layers. **d**, Ratio of the maximum power (P) generated by multilayer membranes to the maximum power generated by a single-layer membrane, for different numbers of layers.

Extended Data Figure 7 | Simulated power generation as a function of membrane thickness.

a

Single-layer MoS$_2$ nanopore

V_+

R_P

Single-layer MoS$_2$ transistor

V_{tg}

D

G

S

V

Single-layer MoS$_2$ nanopore

A

b

c

$V_{tg} = 0.78V$

d

Single-layer MoS$_2$ nanopore

V_{out} R_P

A

R_{load}

V

Extended Data Figure 8 | Characterization of a single-layer MoS$_2$ transistor with nanopores and SMU. a, Electrical measurements with two nanopores (V_+, nanopore output voltage; V_{ds}, drain–source voltage; V_{tg}, top gate voltage). The voltage drop across the transistor channel is monitored with the voltmeter (V); current is measured with current amplifier (A). **b**, Comparison of nanopore measurements with standard two-probe measurements made with an external source. **c**, I–V characteristics at $V_{tg} = 0.78$ V after current stabilization, measured in both set-ups. **d**, Output power of nanopore in Bmim PF$_6$/zinc chloride as a function of load resistance, R_{load}. Inset, circuit diagram for these measurements.

Extended Data Table 1 | Power generation according to membrane thickness

Reverse electrodialysis cells	Power density (W/m^2)	Membrane thickness
Ref. 41	0.17	1 mm
Ref. 42	0.40	3 mm
Ref. 43	0.46	0.19 mm
Ref. 44	0.26	1 mm
Ref. 45	0.95	0.2 mm
Ref. 22	7.7	0.14 mm
Ref. 5	4000	1 μm
This work	10^6	0.65 nm
Multilayer MoS$_2$ (Simulations)	30000	7.2 nm

The table shows the power generated by membranes of different thickness; data from refs 5, 22, 41–45.